Combustion and Flame 242 (2022) 112210

Contents lists available at ScienceDirect

Combustion and Flame

journal homepage: www.elsevier.com/locate/combustflame

Turbulence-induced bias in time-averaged laser absorption tomography of correlated concentration and temperature fields with a first-order correction

Chuyu Wei[a,*], Nikolaos Perakis[b,c], Daniel I. Pineda[d], Fokion N. Egolfopoulos[e], Matthias Ihme[b], R. Mitchell Spearrin[a]

[a] Department of Mechanical and Aerospace Engineering, University of California, Los Angeles, Los Angeles CA 90095, USA
[b] Department of Mechanical Engineering, Stanford University, Stanford CA 94305, USA
[c] Chair of Space Propulsion, Technical University of Munich, Garching 85748, Germany
[d] Department of Mechanical Engineering, The University of Texas at San Antonio, San Antonio, TX 78249, USA
[e] Department of Aerospace and Mechanical Engineering, University of Southern California, Los Angeles CA 90089, USA

ARTICLE INFO

Article history:
Received 11 February 2022
Revised 2 May 2022
Accepted 15 May 2022

Keywords:
Turbulent combustion
Absorption spectroscopy
Large-eddy simulations
Fuel chemistry

ABSTRACT

The influence of correlated scalar fluctuations on time-averaged laser absorption tomography measurements of temperature and species in a piloted turbulent premixed flame was examined using a coupled spectroscopic and fluid-dynamic analysis. To understand bias associated with turbulence, spatio-temporally resolved temperature and species mole fraction profiles predicted by large eddy simulations (LES) were used to synthetically generate time-resolved line-of-sight absorption measurements at short time scales (microsecond) to reflect the unsteady nature of a canonical jet burner across various transverse measurement planes. Inversion methods were employed on the time-averaged line-of-sight data to produce radially-resolved temperature and mole fraction profiles, analogous to those produced by laser absorption tomography performed on a time-averaged axisymmetric flowfield. It is shown that bias in the measurements compared to true time-averaged scalar fields is a function primarily of temperature dependence in absorptivity and non-zero correlation between temperature and species concentration scalars. A first-order correction to tomography measurements is proposed to account for the bias based on estimated correlations and the known spectroscopic parameters of the probed absorption transitions.

1. Introduction

Turbulent combustion provides the primary method of chemical-to-thermal energy conversion in the power generation and transportation sectors, and is expected to be the dominant conversion mechanism in aircraft and rocket propulsion for the foreseeable future [1]. Despite the prevalence of turbulent combustion in practical energy conversion devices, predictive models remain limited. The extraordinarily small spatio-temporal scales of turbulent flames pose unique challenges for both computational and experimental research seeking to increase combustion device performance. To better understand the underlying combustion physics, canonical experimental configurations (e.g., the Sydney/Sandia burners) have been developed to examine turbulent jet flames [2] designed to provide data for model validation under controlled conditions. In such experiments, flow-field measurements of thermochemistry (temperature, molecular species concentration) are desired, but are subject to a multitude of challenges, including rapid temporal fluctuations and multi-dimensionality of the flow-field which may appear convoluted given a finite integration time and sampling point/line-of-sight/view angle. Ultimately, flow-field data should be quantitative to directly compare with state-of-the-art reacting flow models, thus necessitating careful data interpretation when examining turbulent flows.

Owing to their high temporal resolution relative to gas sampling-based methods or thermocouples, optical diagnostics have played a crucial role in the study of turbulent combustion over the last four decades. With increasingly fast-response photodetectors and cameras, methods such as Rayleigh [3–6] and Raman [7–9] scattering, chemiluminescence imaging [10–12], and planar laser-induced fluorescence [13,14] have been employed to

* Corresponding author.
E-mail address: weicy@ucla.edu (C. Wei).

https://doi.org/10.1016/j.combustflame.2022.112210
0010-2180/

Nomenclature

Subscripts and superscripts

$'$	Fluctuating component of a variable
$\bar{}$	Time-averaged component of a variable
$\hat{}$	Measured variable from two-line thermometry
$\vec{}$	Vectors

Symbols

α_ν	Spectral absorbance at wavelength ν
κ_ν	Spectral absorption coefficient at wavelength ν
$A_{j,\text{proj}}$	Projected integrated absorbance area for a rovibrational transition j
K_j	Spatially-resolved integrated absorption coefficient for a rovibrational transition j
S_j	Temperature-dependent linestrength for a rovibrational transition j
$\varphi_{j,\nu}$	Line shape function for a rovibrational transition j
I_t	Transmitted light intensity
I_0	Incident light intensity
l	Spatial location along the line-of-sight
L	Total pathlength along the line-of-sight
t	Time instant
τ	Total time period for averaging
P	Total pressure
L	Temperature of the absorbing gas species
X_{abs}	Mole fraction of the absorbing gas species
$\mathcal{P}(y)$	Projection function in Abel transform
$f(r)$	Radial function in Abel transform
r	Radial location
R	Radius of the flame
$\vec{\mathcal{P}}$	Projection variable vector
$\vec{f}$	Radial variable vector
$\mathbf{A}_{\text{ATP}}$	Three Point Abel transform matrix
$\mathbf{L}_0$	1D discrete gradient matrix
λ	Regularization parameter
R	Ratio of integrated absorption coefficient between two spectral transitions
ϵ	First-order estimate of the correlation-induced bias

assess the flow-field structure and temperature in turbulent flames at time- and length-scales approaching those characteristic of many turbulent flows ($<$ 100 µm, $<$ 100 µs). With appropriate calibrations and/or an estimate of gas composition, these methods can also yield quantitative species concentration measurements [15–17].

Although historically relatively weak in spatial resolution capability owing to its line-of-sight measurement nature, laser absorption spectroscopy (LAS) offers a highly quantitative and calibration-free technique for non-intrusive species and temperature sensing [18]. Aided by advances in compact, portable, low-power, infrared photonics, laser absorption tomography (LAT) has emerged as an imaging technique based on LAS which can readily provide multidimensional distributions of gas properties in flames via multiple line-of-sight spectrally-resolved laser absorption measurements [19]. In recent years, the technique has been applied in the mid-wave infrared to the reaction zones of lab-scale turbulent flames [20–23], yielding quantitative and spatially-resolved time-averaged measurements of species and temperature, which can be compared against state-of-the-art turbulent combustion models [24].

While generally robust to composition variation and many deleterious optical effects, such as thermal emission, particle scattering (sooting), and window fouling, LAT requires the consideration of two prominent sources of error when quantitatively interpreting data collected from turbulent flames: (1) spectral distortion caused by line-of-sight integration through non-uniform thermochemical gradients in the flow-field, and (2) biases in time-averaged spectra caused by correlated temporal fluctuations of flow-field temperature and species concentration. These sources of error have historically received treatment in the context of radio wave propagation affected by atmospheric turbulence [25,26], wherein the temperature and concentration fluctuations are relatively small and optical path-lengths are relatively large compared to those in turbulent flames. Flow-field non-uniformity (1) has been addressed previously with regards to bias on laser absorption measurements [27–32], and recovery via multispectral absorption tomography [33–37]. Accordingly, methods to either mitigate or quantify this type of measurement error have been developed and implemented for presumed steady or quasi-steady flow-fields. However, turbulent flames are highly unsteady, producing fluctuations in steep spatial thermochemical gradients at frequencies that often exceed the effective measurement rates for laser absorption tomography. Time-averaging is commonly employed to increase absorbance signal-to-noise ratio and recover mean field properties. Time-averaging is also inherently required for optical configurations in which the multiple lines of sight are not simultaneously acquired [36,38,39]. Such time-averaging of the absorption spectra introduces potential measurement error (2) owing to both the non-linear relationship of absorption linestrength with temperature as well as fluctuations in flow-field temperature and mole fraction. To mitigate this error, Emmert et al. [22] developed a fluctuation model to both estimate and correct for the biases in time-averaged LAT measurements made in a swirled oxy-fuel coal combustor, comparing their corrected measurements with O_2-CARS measurements in the flow. The authors assumed that fluctuations in temperature and species concentration were independent, and that the temperature fluctuations could be described by a normal distribution, which was determined by fitting an additional standard deviation parameter in the reconstruction process. However, in combustion, temperature changes are highly correlated with the production of CO_2 and H_2O, as well as both the production and consumption of CO, amongst other species. In a prior paper investigating fuel effects in piloted premixed jet flames [24], we have utilized large eddy simulations to quantify the potential error associated with correlated fluctuations of temperature and mole fraction of CO and CO_2 under specific conditions; however, we stopped short of attempting to correct for the biases.

In this work we rigorously examine turbulence-induced biases in time-averaged line-of-sight absorption measurements, with the aim of providing a broadly applicable framework to mitigate such biases and increase the accuracy of LAT measurements in turbulent flames. To do this, we leverage large eddy simulations to computationally perform synthetic laser absorption tomography on a simulated piloted premixed ethylene-air turbulent jet flame, predicting spatially-resolved temperature and concentration measurements in the flow-field. We then compare time-averaged measurements with mean values determined directly from the LES predictions and quantify the measurement biases with respect to correlated flow-field scalars and turbulence intensity. Notably, we develop a first-order correction for the measurement biases and characterize its performance over the range of turbulence intensities observed in these flames. We examine the correction method assuming a variety of different spectral transition pairs, and suggest a line selection best suited for minimizing measurement errors in turbulent reacting flows. Lastly, we apply the correction method to experimental laser absorption tomography measurements made on a turbulent jet burner and compare with LES predictions.

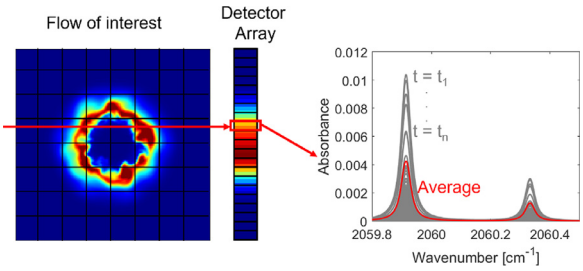

Fig. 1. *Left:* 2D spectral absorption coefficient κ_ν field for an instantaneous timestep t in a turbulent flame; *Middle:* 1D array of spectral absorbance α_ν calculated from κ_ν integrated over pathlength L; *Right:* α_ν as a function of wavenumber ν for several timesteps (gray) alongside time-averaged value (red). (For interpretation of the references to colour in this figure legend, the reader is referred to the web version of this article.)

2. Theory and methods

2.1. Laser absorption spectroscopy

Laser absorption spectroscopy (LAS) exploits resonance with discrete energy modes of gas molecules to ascertain thermochemical properties of flow fields from light absorption [40]. The Beer-Lambert law provides the spectrally-dependent absorbance α_ν in a gas medium along a line-of-sight l [cm] for a specific frequency ν [cm^{-1}] as a function of the ratio of incident light, I_0, and the transmitted light, I_t, of a light source through the gas:

$$\alpha_\nu = -\ln\left(\frac{I_t}{I_0}\right)_\nu = \int_0^L \kappa_\nu(l)\mathrm{d}l = \int_0^L PS_j(T(l))X_{\mathrm{abs}}(l)\varphi_{j,\nu}\mathrm{d}l\,, \quad (1)$$

where α_ν depends on the line-of-sight-integration of the spectral absorption coefficient, κ_ν [cm^{-1}], which is dependent on total pressure P [atm], temperature-dependent linestrength $S_j(T(l))$ [cm^{-2}/atm] and lineshape function $\varphi_{j,\nu}$ [cm] for spectral transition j, mole fraction of absorbing species $X_{\mathrm{abs}}(l)$, and aggregate pathlength L [cm]. Although pressure is assumed constant, $T(l)$ and $X_{\mathrm{abs}}(l)$ have a spatial dependence on position l within the aggregate pathlength L, as the flow is not presumed to be spatially uniform, which is shown in the left of Fig. 1.

In scanned-wavelength direct absorption spectroscopy (scanned-DA), the laser light source is repeatedly modulated rapidly in time across a wavelength interval encompassing one or more spectral transitions, allowing for the elimination of the dependence on spectral lineshape ($\int_{-\infty}^{\infty}\varphi_{j,\nu}\mathrm{d}\nu = 1$) [18]. This is especially advantageous for in-situ measurements of flames, as $\varphi_{j,\nu}$ is dependent on both $T(l)$ and non-absorbing gas mixture composition $X(l)$, which are not usually known a priori. A representative wavelength range encompassing two transitions of carbon monoxide is shown in the right of Fig. 1. By integrating over the wavenumber domain, the projected integrated absorbance area $A_{j,\mathrm{proj}}$ for a rovibrational transition j can be obtained as:

$$A_{j,\mathrm{proj}} = \int_{-\infty}^{\infty}\alpha_\nu d\nu = \int_0^L K_j\mathrm{d}l = \int_0^L PS_j(T(l))X_{\mathrm{abs}}(l)\mathrm{d}l\,, \quad (2)$$

where K_j [cm^{-2}] is the spectrally-integrated absorption coefficient for a rovibrational transition j, and is obtained by integrating κ_ν over the wavenumber domain of that transition. K_j and κ_ν are analogous to $A_{j,\mathrm{proj}}$ and α_ν, respectively, with the former pair corresponding to local quantities associated with the differential pathlength $\mathrm{d}l$, while the latter pair corresponds to the path-integrated quantities over the aggregate pathlength L. These latter quantities are directly calculated with the intensity values measured by detectors in an experiment, while the former quantities must be indirectly determined, as discussed in the next subsection.

2.2. Time-averaged laser absorption tomography

Equations (1) and (2) hold for steady or unsteady flowfields. However, turbulent flames are highly unsteady with temporal fluctuations on the order of 1–10 kHz. For such flows, time-averaging may be used by necessity or by desire to recover mean properties. In this case, the Beer-Lambert law can be written in a time-averaged form over a time period τ:

$$\begin{aligned}\overline{\alpha}_\nu &= \frac{1}{\tau}\int_0^\tau \alpha_\nu(t)\mathrm{d}t = \int_0^L \overline{\kappa}_\nu(l)\mathrm{d}l\,,\\ &= \frac{1}{\tau}\int_0^\tau\int_0^L \kappa_\nu[T(t,l), X_{\mathrm{abs}}(t,l)]\mathrm{d}l\mathrm{d}t\,, \end{aligned} \quad (3)$$

where $\overline{\alpha}_\nu$ and $\overline{\kappa}_\nu(l)$ are the measured time-averaged spectral absorbance and spatially-resolved time-averaged spectral absorption coefficient along the line-of-sight, respectively. Examples of instantaneous and time-averaged absorbance spectra through a simulated turbulent flame are shown in the right panel of Fig. 1.

Similarly, the time-averaged integrated absorbance area $\overline{A}_{j,\mathrm{proj}}$ can be obtained by integrating the time-averaged spectra over the wavenumber domain:

$$\overline{A}_{j,\mathrm{proj}} = \int_{-\infty}^{\infty}\overline{\alpha_\nu}d\nu = \int_0^L \overline{K}_j(l)\mathrm{d}l = \int_0^L P\overline{S_j(T(l))X_{\mathrm{abs}}(l)}\mathrm{d}l\,, \quad (4)$$

where the total pressure is assumed to be constant and $\overline{K}_j(l)$ is the spatially-resolved time-averaged integrated absorption coefficient along the line-of-sight.

In time-averaged LAT, the spatial profile of the average absorption coefficient $\overline{\kappa}_\nu$ or $\overline{K}_j$ is determined from averaged projected measurements $\overline{\alpha}_\nu$ or $\overline{A}_{j,\mathrm{proj}}$ using tomographic reconstruction methods. To simplify the analysis, we assume the time-averaged flowfield is axisymmetric and steady, and therefore one-dimensional tomographic reconstruction methods can be applied. We further focus on the spectrally integrated absorption $\overline{A}_{j,\mathrm{proj}}$ and $\overline{K}_j$ to eliminate the complex nonlinear dependence of the lineshape function on flow composition and temperature. It should be noted that the simplified 1D analysis and subsequent first-order correction (discussed in Section 2.4) can be extended in theory to 2D non-axisymmetric flowfields [41]. Under the axisymmetric assumption, the projected absorbance area measurement can be described by the well-known Abel transform as a line-of-sight integration over the flame with radius R:

$$\mathcal{P}(y) = 2\int_y^R \frac{f(r)r}{\sqrt{r^2-y^2}}dr\,, \quad (5)$$

where $\mathcal{P}(y)$ is the measured time-averaged projected absorbance area $\overline{A}_{j,\mathrm{proj}}(y)$ at a given distance from the flame center y and $f(r)$ is the radial distribution of the time-averaged spectrally-integrated absorption coefficient $\overline{K}_j(r)$.

In practice, Abel inversion is implemented numerically [42]; the flame region is divided into equally spaced annular rings and the radial distribution $f(r)$ is approximated by a quadratic function near radius r using the Abel 3-point (ATP) method [43]. Under this approximation, Eq. (5) can be written in terms of a system of linear equations represented by

$$\mathbf{A}_{\mathrm{ATP}}\vec{f} = \vec{\mathcal{P}}\,, \quad (6)$$

where $\vec{f} = [f_0, f_1, \ldots f_{N-1}]^T$ and $\vec{\mathcal{P}} = [\mathcal{P}_0, \mathcal{P}_1, \ldots \mathcal{P}_{N-1}]^T$ contain values of $\overline{K}_j(r)$ and $\overline{A}_{j,\mathrm{proj}}(y)$, respectively, at every radial location. To address the inherently ill-conditioned nature of the projection matrix $\mathbf{A}_{\mathrm{ATP}}$, we adopted Tikhonov regularization [42] to find the radial distribution $f(r)$ from a least-squares solution:

$$\vec{f}_\lambda = \arg\min\left\|\begin{bmatrix}\mathbf{A}_{\mathrm{ATP}}\\ \lambda\mathbf{L}_0\end{bmatrix}\vec{f} - \begin{bmatrix}\vec{\mathcal{P}}\\ 0\end{bmatrix}\right\| \quad (7)$$

where $\mathbf{L}_0$ is a discrete gradient matrix that characterizes the smoothness of the solution; λ is the regularization parameter that controls the relative importance of the accuracy and smoothness of the solution and a suitable regularization parameter is determined from the *L*-curve method [42,44]. The technique described above enables the reconstruction of the radial profiles of integrated spectral absorption coefficient, $\overline{K_j}(r)$, from the measured time-averaged projected absorbance areas, $\overline{A_{j,\mathrm{proj}}}(y)$. For multiple transitions j scanned, multiple $\overline{K_j}(r)$ can be determined, the ratios of which can be expressed as a ratio of linestrengths and thus a function of temperature only, as shown by the following equation [18]:

$$R(r) = \frac{\overline{K}_A(r)}{\overline{K}_B(r)} = \frac{P\hat{X}_{\mathrm{abs}}(r)S_A(\hat{T}(r))}{P\hat{X}_{\mathrm{abs}}(r)S_B(\hat{T}(r))} = \frac{S_A(\hat{T}(r))}{S_B(\hat{T}(r))} = f(\hat{T}(r)) \,, \tag{8}$$

where $S_j(T)$ can be calculated using information readily available in spectral databases [45], thus enabling the quantitative determination of an inferred temperature $\hat{T}$. After $\hat{T}$ has been determined, the inferred mole fraction of the absorbing species $\hat{X}_{abs}$ can be obtained using the following relation for the known pressure P:

$$\hat{X}_{\mathrm{abs}}(r) = \frac{\overline{K}_j(r)}{PS_j(\hat{T}(r))} \,, \tag{9}$$

Implicit in these final calculation steps is that the inferred temperature $\hat{T}$ and mole fraction $\hat{X}_{\mathrm{abs}}$ determined from time-averaged absorption coefficients are also the true time-averaged values, $\overline{T}$ and $\overline{X}_{\mathrm{abs}}$. However, as we will show and discuss further, correlated temperature and mole fraction fluctuations may bias such an inference. Generally, this is because the measured time-averaged absorption coefficient $\overline{K_j}$ does not necessarily equal the absorption coefficient based on time-averaged temperature and mole fraction; that is, $\overline{K_j(T, X_{\mathrm{abs}})} \neq K_j\left(\overline{T}, \overline{X}_{\mathrm{abs}}\right)$. The key factors driving this bias are examined through a first-order analysis in Section 2.4 and via numerical simulations of turbulent jet flames in Section 3. We next describe the detailed turbulent flame simulations used to make such an assessment.

2.3. Large eddy simulations

The turbulent flame configuration examined here is based on the canonical Sydney/Sandia burners [5,11,46], wherein a piloted premixed jet flame is thermally insulated by a hot co-flow so that turbulence-chemistry interactions can be investigated while removing other complexities arising from heat losses and entrainment effects. This subsection describes our methods for both simulating and analyzing the flowfield scalars produced by this canonical experimental configuration in the context of simulated laser absorption tomography measurements.

To obtain flowfield quantities that capture correlated fluctuations based in combustion physics, reacting LES are performed to predict the temporally- and spatially-resolved temperature and mole fraction fields of a piloted premixed turbulent flame fueled by ethylene (C_2H_4) and air at a fuel-air equivalence ratio of $\phi = 0.55$, surrounded by a hot co-flow of H_2-air products at approximately 1500 K. The details of the simulations are provided in previous work [24], but key aspects of the numerical setup are briefly reviewed here for reader clarity. The turbulent reacting flowfield is obtained as solution to the Favre-filtered conservation equations for mass, momentum, total energy, and species [24], and the turbulent combustion is modeled using a finite-rate chemistry model. For the subgrid-scale turbulence-chemistry interaction, the Vreman model [47] is used to represent the turbulent subgrid stresses, and the dynamic thickened-flame model [48] is employed with a maximum thickening factor of 3. The source term of CO is used as a sensor in which the maximum net production rate of CO in a free flame simulation is employed as a threshold for the activation of the thickened-flame model [24].

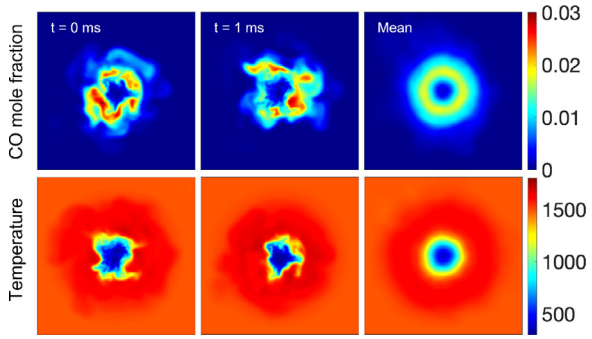

Fig. 2. Instantaneous flowfields for CO mole fraction (top) and temperature (bottom) predicted by the LES at t =0 ms (left), t =1 ms (middle), and mean values over 5 ms (right), at a flame height of $x/D = 12.5$.

A finite-volume formulation is employed to discretize the governing equations [49,50]. The convective fluxes are discretized using a hybrid method, which combines a central scheme with a second-order essentially non-oscillatory scheme. A simpler splitting scheme is employed to separate the convection, diffusion, and reaction operators [51]. A strong stability-preserving 3rd-order Runge-Kutta (SSP-RK3) scheme [52] is used for time-integration of non-stiff operators, and the reaction chemistry is integrated using a semi-implicit Rosenbrock-Krylov scheme [51], having a computational cost that scales linearly with the number of species in the mechanism.

The chemical kinetic mechanism employed in these simulations, based on USC Mech II [53], is DRG-reduced [54] and validated against calculations [55] of 1D laminar flames with S_L, temperature profiles, and major species profiles as reduction targets, as described in previous work [24]. The performance of this reduced mechanism with respect to species profiles in laminar flames, laminar flame speed, and ignition delay is also described in further detail in prior work [24].

The dimensions of the three-dimensional computational domain are 0.35 m $\times$ 0.26 m $\times$ 2π in the axial, radial, and azimuthal directions, respectively. The grid uses 401 non-uniformly distributed points in the axial direction, concentrated in the vicinity of the injection plane to ensure sufficient resolution of the turbulent shear layer. The axial resolution directly downstream of the injection plane has a mesh resolution of 93 μm with a growth ratio of 0.65% for the domain within the first two jet diameters downstream of the inlet. The radial direction is discretized with 125 points, clustered in the shear layers between the streams of the central jet, the pilot flame, and the hot co-flow, while 160 points are used for the circumferential resolution. At the inlet of the jet stream, a turbulent velocity profile is applied, with turbulent fluctuations prescribed to match the experimentally measured velocity field. For the co-flow and pilot streams, the velocity corresponding to the burnt products along with the adiabatic chemical equilibrium temperature and composition is prescribed.

The LES computations provide spatially-resolved instantaneous thermochemical properties (temperature, mole fractions) for the C_2H_4-air turbulent flame under investigation. Representative instantaneous planar flowfields for CO and temperature predicted by these simulations for the jet flame are shown in Fig. 2. For comparison with the experimental laser absorption tomography measurements—which represent time- and azimuthally-averaged thermochemistry—the simulations are run for five convective flow-through times, and averaged flowfield results are obtained by averaging both in time and in azimuthal direction. For each flame, a subset of time-resolved (subsampled at $\Delta t = 7$ μs) instantaneous thermochemical profiles along a single line of sight at various x/D were used for quantifying the influence of correlated variable fluc-

tuations on the LAT measurements, as described in the next subsection.

2.4. First-order analysis and correction

As discussed, turbulent flames are highly unsteady reacting flowfields with temporal fluctuations on the order of 1–10 kHz, necessitating time-averaging for most scanned-wavelength absorption techniques. It is desirable to compare measurements of turbulent flame thermochemistry with predictions offered by state-of-the-art models; however, the measured and simulated quantities must be directly comparable. In this study, we seek to compare time-averaged measurements of spatially-resolved thermochemistry based on laser absorption tomography with time- and azimuthally-averaged predictions by large-eddy simulations. Turbulence-induced thermochemical fluctuations in both the experiments and numerical simulations—particularly those resulting in correlated flowfield scalars [56]—can influence our ability to make direct comparisons of these averaged values. To assess the magnitude of these influences and establish a basis for a first-order correction, we decompose the instantaneous absorption coefficient K_j in Eq. (2) into its mean and fluctuation, $\overline{K}_j$ and K'_j, respectively:

$$K_j = \overline{K}_j + K'_j = P\left(a\overline{T} + aT' + b\right)\left(\overline{X}_{\text{abs}} + X'_{\text{abs}}\right) \tag{10}$$

where the temperature-dependent linestrength $S_j(T)$ is expressed via a first-order Taylor expansion $S_j(T) = aT + b$, and mole fraction X and temperature T are each decomposed into their mean ($\overline{X}$ and $\overline{T}$) and fluctuation (X' and T') values. Although $S_j(T)$ is typically nonlinear with temperature [40], this expression illustrates the influence of correlated flowfield scalars on the time-averaged measurement. We can take the mean of Eq. (10) and assume that the mean of each fluctuation is zero to obtain:

$$\overline{K}_j = PS_j\left(\overline{T}\right)\overline{X}_{\text{abs}} + aP\overline{T'X'_{\text{abs}}} \tag{11}$$

where a is the slope of the linestrength with respect to temperature at the averaged temperature, $\partial S_j(T)/\partial T|_{\overline{T}}$. In Eq. (11), $\overline{T'X'_{\text{abs}}}$ represents the time-averaged correlation between the turbulent fluctuations in temperature and mole fraction, which cannot be assumed as zero if T' and X'_{abs} are not independent. Although we have ignored higher-order terms in the Taylor expansion of the non-linear $S_j(T)$, Eq. (11) clearly shows that in turbulent flows where $\overline{T'X'_{\text{abs}}}$ is expected to be large,

$$\overline{K_j(T, X_{\text{abs}})} \neq K_j\left(\overline{T}, \overline{X}_{\text{abs}}\right) \tag{12}$$

Although experimentally determined values of $\overline{K}_j$ determined by LAT of turbulent flames are convoluted by correlated scalars, we can use the second term in Eq. (11) to predict—to a first-order estimate—measurement biases in the turbulent flame based on spatio-temporally resolved X_{abs} and T provided by LES predictions. For any point (x, r) in the turbulent flowfield, we can define $\epsilon(x, r)$, a first-order estimate of the measurement bias in $\overline{K}_j(x, r)$ caused by correlated fluctuations of temperature and mole fraction, from Eq. (11):

$$\epsilon(x, r) = aP\overline{T'X'_{\text{abs}}} = \left.\frac{\partial S_j(T)}{\partial T}\right|_{\hat{T}} \cdot P \cdot \frac{1}{\tau}\int_0^{\tau} T'X'_{\text{abs}}dt \tag{13}$$

The partial derivative of temperature-dependent linestrength with respect to temperature, $\partial S_j(T)/T|_{\hat{T}}$, can be determined using information in spectral databases, and is evaluated numerically at the uncorrected inferred temperature $\hat{T}$ determined using Eq. (8). Equation (13) provides a first-order correction for the measurement bias in $\overline{K}_j$ caused by $\overline{T'X'_{\text{abs}}}$. Example time-histories of $\overline{T'X'_{\text{abs}}}$ at particular locations (x, r) in the flowfield of the turbulent jet flame are shown in Fig. 3 for the target absorbing species, CO,

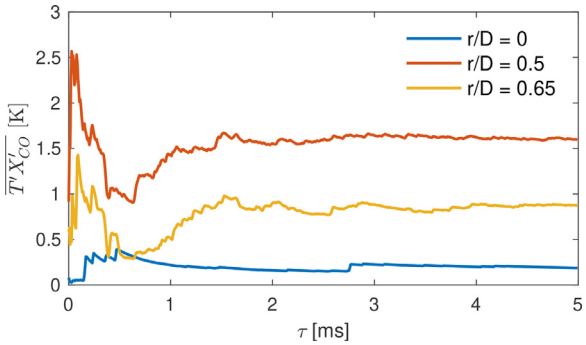

Fig. 3. Representative time histories of the correlation term for the plane of $x/D = 12.5$.

wherein the cumulative averages of $T'X'_{\text{abs}}$ are plotted as a function of time over a 5 ms interval using Eq. (13). It can be seen that as the simulation time interval τ increases, $\overline{T'X'_{\text{abs}}}$ approaches a constant value with which we can estimate the measurement bias in $\overline{K}_j$.

3. Results and analysis

This section describes the resulting measurement bias for the aforementioned turbulent jet flame, using the methods presented in the previous section, as well as analysis of a first-order correction. The laser absorption analysis is performed using a group of P-branch transitions from the fundamental vibrational band of carbon monoxide near 5 μm; pairs of these transitions have previously been used for thermometry in flames [20,57]. First, we demonstrate the turbulence-induced bias in a simulated local spectra based on the time history of mole fraction and temperature fluctuations from the LES results. Then, we quantify the sensitivity of the turbulence-induced bias in simulated absorption measurements of mole fraction and temperature to varying intensity of radially-resolved $\overline{T'X'_{\text{abs}}}$. Additionally, we apply the first-order correction provided by Eq. (13) on the simulated absorption data, using $\overline{T'X'_{\text{abs}}}$ provided by LES predictions to produce spatially-resolved $\overline{T}$ and $\overline{X}_{\text{abs}}$ which are closer to the true means predicted by LES. We examine the influence of spectral transition choice on the bias and the performance of the first-order correction. Lastly, we apply the first-order correction to real measurements on a turbulent jet burner and compare to LES predictions of the same flame.

3.1. Effect of correlated scalar fluctuations

It is important to first recognize that turbulence-induced thermochemical fluctuations in turbulent flames exhibit correlated flowfield scalars [56] and the manner in which this affects spectral data. To demonstrate the influence of this correlated fluctuation on the local spectra, the absorption coefficient of two carbon monoxide transitions near 2060 cm^{-1} is simulated using a representative 5-ms time history of temperature and CO mole fraction from reacting flow Large Eddy Simulations as shown in Fig. 4. Notably, the zoomed inset reveals a clear positive correlation between temperature and CO fluctuations at this location.

First, an instantaneous spectral absorption coefficient, $\kappa_\nu[T(t), X_{\text{abs}}(t)]$, is simulated at every time step ($\Delta t = 7\ \mu\text{s}$), and the time-averaged spectral absorption coefficient $\overline{\kappa}_\nu$ is subsequently determined using Eq. (3) and is shown as a solid line in Fig. 5. Additionally, the spectral absorption coefficient based on the time-averaged temperature $\overline{T}$ and mole fraction $\overline{X}_{\text{abs}}$, $\kappa_\nu[\overline{T}, \overline{X}_{\text{abs}}]$, is simulated and shown as a dashed line in Fig. 5. The time-averaged spectral absorption coefficient $\overline{\kappa}_\nu$, representing a simulated LAT

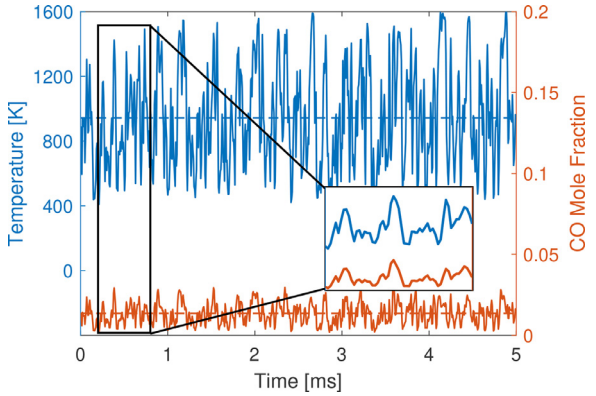

Fig. 4. Representative time history of the LES-predicted temperature and CO mole fraction with a correlation of $\overline{T'X'_{CO}} = 1.87$ K at a location in the flame corresponding to $x/D = 12.5$ and $r/D = 0.5$. Dashed lines indicate the time-average values.

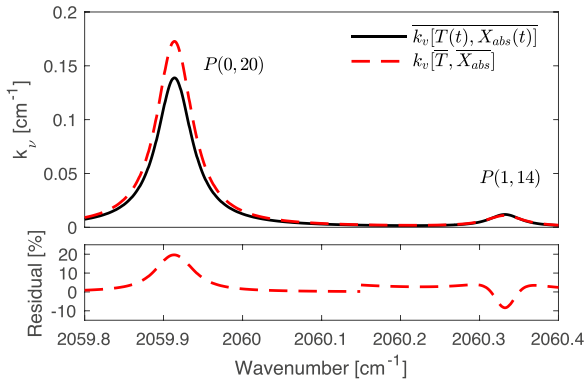

Fig. 5. Spectral absorption coefficient κ_ν for the P(0,20) and P(1,14) transitions of CO assuming time-averaged values (solid line) and assuming time-averaged values of X_{CO} and T (dashed line), with corresponding residual below.

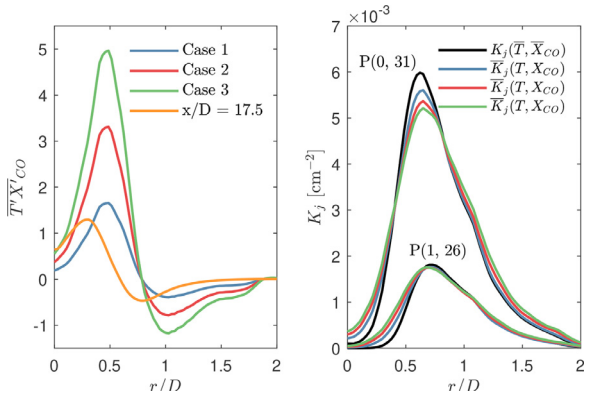

Fig. 6. Radial profiles of the correlation term (*left*) and corresponding biases in absorption coefficients $\overline{K}_j$ (*right*) for the plane at $x/D = 12.5$.

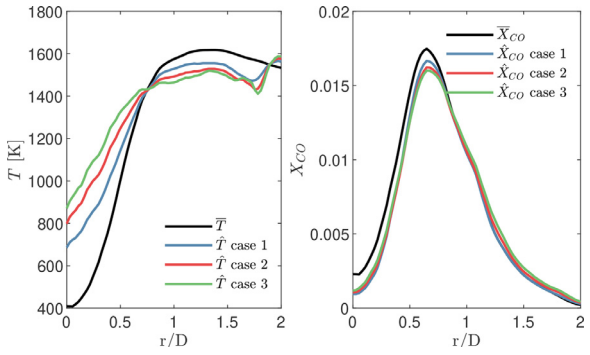

Fig. 7. Radially-resolved values of $\hat{X}_{CO}$ calculated by Eq. (9) using the multiple profiles of $\overline{K}_j$ shown in Fig. 6 and the corresponding temperatures $\hat{T}$ shown in Fig. 7 in the $x/D = 12.5$ plane.

measurement, is significantly different from the spectral simulations performed assuming time-averaged conditions. For the P(0,20) CO transition, the absorption peak of the time-averaged simulation is 20% lower than that of the simulation performed with time-averaged conditions and the overall lineshape is also broader. The opposite bias is observed for the P(1,14) transition. Accordingly, the time-averaged integrated absorption coefficient $\overline{K}_j$ will also be biased by the time-averaging, which will lead to biased temperature and mole fraction results if two-line thermometry is directly applied. This biasing effect is a result of the strong temperature dependence of the linestrength $S_j(T)$ and lineshape function $\varphi_{j,\nu}$, and the correlation between the temperature and mole fraction fluctuations $\overline{T'X'_{\text{abs}}}$, as mentioned in Section 2. Notably, the fluctuation of species with temperature will bias the spectra to reflect a temperature that is more often exhibited at times when the absorbing species number density is high. As such, temperature $\hat{T}$ and mole fraction $\hat{X}_{\text{abs}}$ determined from two-line thermometry can be clearly biased from the actual time-averaged flowfield temperature $\overline{T}$ and mole fraction $\overline{X}_{\text{abs}}$.

3.2. Effect of correlation magnitude

Here, we further examine the influence of the magnitude of the correlated fluctuations in flow-field scalars on the measurement bias in $\hat{T}$ and $\hat{X}_{\text{abs}}$ by scaling the flow-field fluctuations of the LES predictions about the spatially-resolved mean values by multiple magnitudes and measurement locations, shown in the left of Fig. 6. Case 1 represents the radial distribution of $\overline{T'X'_{\text{abs}}}$ directly from LES simulation at plane $x/D = 12.5$. Cases 2 and 3 represent synthetic profiles created by scaling Case 1 by factors of 2 and 3, respectively. Additionally, the radial distribution of $\overline{T'X'_{\text{abs}}}$ at plane $x/D = 17.5$ is also plotted to demonstrate the correlation level across the flow field. Generally, the radial profiles have a similar distribution with a positive correlation near the center of the flame and a negative correlation in the outer region. As the axial location increases, the peak correlation location moves towards the flame center and the peak value decreases.

1 D profiles of time-averaged projected absorbance area $\overline{A}_{j,\text{proj}}$ are generated using Eq. (4) based on time histories of temperature and mole fraction in each case, which are then Abel-inverted to determine the time-averaged $\overline{K}_j$ for two representative ro-vibrational transitions of CO, $P(0, 31)$ and $P(1, 26)$. The corresponding radially-resolved profiles of $\overline{K}_j$ are shown in the right of Fig. 6 alongside K_j calculated using the 'true' $\overline{T}$ and $\overline{X}_{\text{abs}}$ predicted by the LES.

It can be noted that increasing the magnitudes of $\overline{T'X'_{\text{abs}}}$ has a broadening or dispersion effect on the radial profiles of $\overline{K}_j$, particularly for the P(0,31) ro-vibrational transition. The peak values of $\overline{K}_j$ decrease, while the steepness of the gradients on either side of the peaks reduce, especially near the centerline of the flow-field. Although the effect on each $\overline{K}_j$ relative to their true K_j appears small overall, the ratios of $\overline{K}_j$ for each ro-vibrational transition—particularly at certain radial positions—are more significantly affected, rendering a pronounced influence on the temperature determined using Eq. (8), as can be seen in Fig. 7.

Absolute deviations in temperature from the 'true' value, $|\hat{T} - \overline{T}|$, approach 200 K in the outer regions of the flame, and nearly 500 K in the centerline of the flame for Case 3 (with the highest correlated fluctuations). Notably, the correlation term $\overline{T'X'_{\text{abs}}}$ approaches zero around $r/D = 0.8$, which corresponds to the ra-

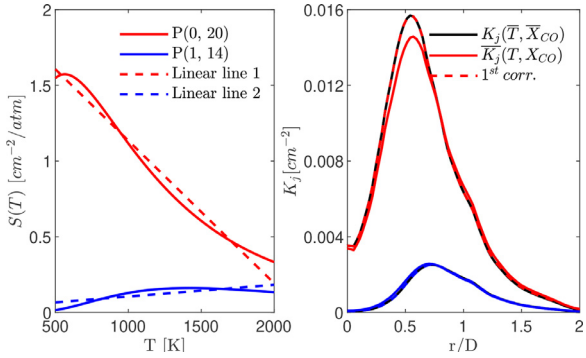

Fig. 8. Calculated values of $K_j(\overline{T},\overline{X}_{abs})$ using time-averaged thermochemical data predicted by LES alongside the time-averaged values of $\overline{K}_j$ in the plane at $x/D = 12.5$ for synthetic linear lines.

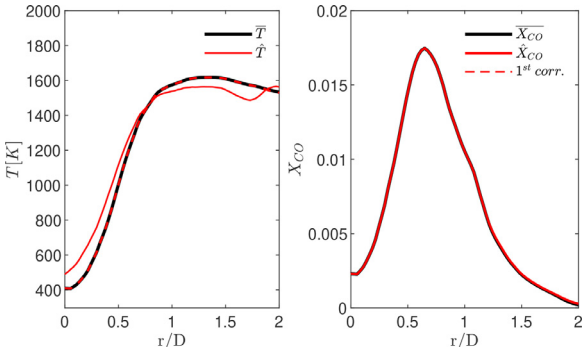

Fig. 9. Time-averaged temperature $\overline{T}$ and CO mole fraction $\overline{X}_{CO}$ predicted by LES alongside the uncorrected and corrected values $\hat{T}$ and $\hat{X}_{CO}$ in the plane at $x/D = 12.5$ using synthetic linear lines.

dial location where inferred temperature $\hat{T}$ and mole fraction $\hat{X}_{CO}$ are not biased from the time-averaged values $\overline{T}$ and $\overline{X}_{abs}$. This is because when the term $\overline{T'X'_{abs}}$ approaches zero, absorption coefficients K_j are not biased based on the first-order analysis of Eq. (11), i.e. $\overline{K_j(T,X_{abs})} \approx K_j(\overline{T},\overline{X}_{abs})$. Additionally, the first-order analysis is also able to provide the direction change of the bias around $r/D = 0.8$ based on the sign of the correlation term $\overline{T'X'_{abs}}$.

The effect on mole fraction is less pronounced, as shown in the right Fig. 7, owing to its linear relationship with K_j. Both the peak 'measured' mole fraction $\hat{X}$ as well as the values of $\hat{X}$ near the center of the flame are systematically lower than the 'true' mole fraction $\overline{X}$, while the outer regions of the flame are much less affected. Unlike for the simulated $\hat{T}$, the severity of the correlated fluctuations does not readily distinguish the mole fraction profiles from one another.

3.3. Demonstration of the first-order correction

Here, we demonstrate the first-order correction developed in Section 2.4 based on two synthetic transitions with assumed perfect linear temperature dependencies, to correct for the turbulence-induced biases in temperature and species shown in previous sections. The synthetic linear lines are generated by linearly fitting the P(0,20) and P(1,14) ro-vibrational transitions of the fundamental bands of carbon monoxide [57] over the range between 500 K and 1600 K, as shown in the left of Fig. 8.

The corresponding time-averaged profiles of $\overline{K}_j$ for each ro-vibrational transition based on Case 1 (discussed in Section 3.2) are shown in the right of Fig. 8 alongside values of the absorption coefficient evaluated at the averaged temperature and mole fraction, $K_j(\overline{T},\overline{X}_{abs})$ for the same plane of $x/D = 12.5$. Additionally, a first-order correction is applied to the synthetic transitions using Eq. (11) based on the radially-resolved $\overline{T'X'_{abs}}$ in Fig. 6 and the slopes of the corresponding linear linestrengths.

The time-averaged values of $\overline{K}_j$ are affected most prominently around $r/D = 0.5$ where the correlation term $\overline{T'X'_{abs}}$ is maximum, as the bias in $\overline{K}_j$ scales linearly with $\overline{T'X'_{abs}}$. It is also noted that the first-order correction to $\overline{K}_j$, evaluated by Eq. (13), completely corrects for the bias created by the time-averaged correlated fluctuations $\overline{T'X'_{abs}}$ when applied to the simulated measurement of $\overline{K}_j$. This is expected, since the correction term was generated using a first-order Taylor series expansion of $\overline{K}_j$ and the linestrengths used to calculate these simulated absorbance fields are linearized approximations.

The profiles of LES-predicted true mean temperature $\overline{T}$ alongside the inferred temperatures $\hat{T}$ calculated using Eq. (8) with the uncorrected and corrected $\overline{K}_j$ profiles are shown in the left of Fig. 9.

Notably, when the ratio of the two corrected $\overline{K}_j$ is used, the true temperature profile $\overline{T}$ is recovered. The profiles of LES-predicted true mean mole fractions $\overline{X}_{CO}$ alongside the mole fractions $\hat{X}_{CO}$ calculated from Eq. (9) using the uncorrected and corrected $\overline{K}_j$ and $\hat{T}$ profiles are shown in Fig. 9. It should be noted that for the line pair comprising two perfectly linear lines, the uncorrected $\hat{X}_{CO}$ are not biased from the actual time-averaged profile $\overline{X}_{CO}$, unlike the case using the nonlinear line pair comprising the P(0,31) and P(1,26) ro-vibrational transitions, as shown in Fig. 7. This is consistent with previous work by Goldenstein et al. [28] demonstrating that for flow non-uniformity, the column density—or the path-averaged concentration—can be recovered using transitions with approximately linear dependence on temperature. This also highlights the importance of wavelength selection for accurately assessing the spatially-resolved time-averaged thermochemistry of the flowfield, as is discussed in the following subsection. Since the bias in mole fraction can be largely eliminated by leveraging spectral transitions with approximately linear temperature dependence, we will focus the discussion on the temperature correction in the following subsections.

3.4. Line pair selection

Line selection criteria for two-line thermometry have been well-discussed in the context of steady uniform flows [58] as well as spatially non-uniform flows [28]. In this subsection, we make additional consideration of the unsteady fluctuations and associated bias in inferred temperature for turbulent flows as well as the performance of the subsequent first-order correction, with a specific focus on the P-branch CO lines of interest. Four CO ro-vibrational transitions in the fundamental band are selected to form three line pairs; their respective spectroscopic parameters are listed in Table 1. Line pair A and B are selected to have a similar lower-state-energy difference $\Delta E''$ while line pair C has a higher $\Delta E''$.

Table 1
Spectroscopic parameters of the selected transitions in this work.

Line Pair	Line (ν'', J'')	Freq. [cm^{-1}]	E'' [cm^{-1}]	S (296 K) [cm^{-2}/atm]
A	P(1,14)	2059.91	2543	2.64×10^{-6}
	P(0,20)	2060.33	806	8.76×10^{-1}
B	P(1,26)	2006.78	3478	5.20×10^{-6}
	P(0,31)	2008.53	1901	6.62×10^{-3}
C	P(1,26)	2006.78	3478	5.20×10^{-6}
	P(0,20)	2060.33	806	8.76×10^{-1}

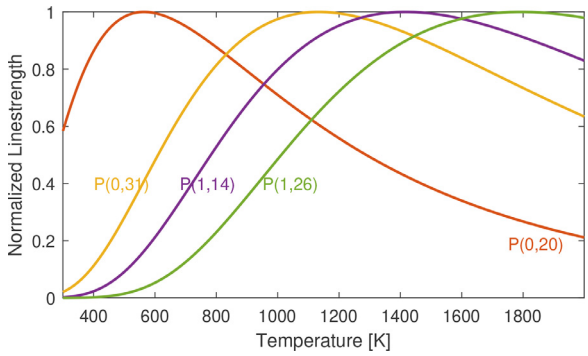

Fig. 10. Normalized linestrength of selected transitions as a function of temperature.

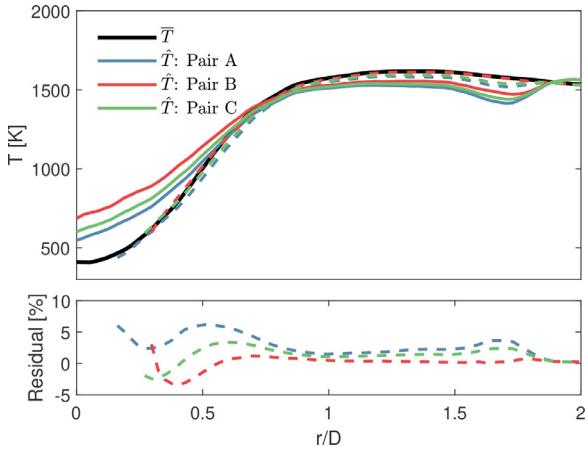

Fig. 11. Time-averaged temperature $\overline{T}$ predicted by LES alongside the uncorrected and corrected values $\hat{T}$ in the plane at $x/D = 12.5$ using three different line pairs.

The lower state energies (E'') of the four transitions were well-distributed in order to examine transitions with different temperature dependencies while ensuring high temperature sensitivity. The normalized linestrengths of those transitions are plotted as a function of temperature in Fig. 10. Generally, the linestrength increases with temperature initially, then plateaus and decays, scaling approximately linearly with temperature on each side of the peak. Additionally, a larger lower-state energy E'' shifts the linestrength peak to a higher temperature with a broader plateau region.

The profiles of LES-predicted true mean temperature $\overline{T}$ alongside the uncorrected and corrected temperatures $\hat{T}$ calculated using different line pairs are shown in Fig. 11. Significant biases in temperature from $\overline{T}$ are observed near the centerline of the flame, with an absolute temperature deviation approaching 300 K for line pair B. Notably, while line pairs A and B have similar lower state energy differences, the bias in the centerline is nearly doubled for line pair B. Line pair C, despite possessing the highest temperature sensitivity, does not provide the smallest bias of the line pairs examined. This highlights the need to consider additional factors when measuring turbulent flows with highly correlated scalar fields. A key factor to consider is the linearity of the linestrength over the range of the temperature fluctuation. This is examined by considering the percentage change in linestrength from its value at mean temperature as a function of the temperature deviation $\Delta T = T - \overline{T}$, as shown in Fig. 12 for two representative mean temperatures. Notably, around a mean temperature $\overline{T} = 1000$ K, the linestrength of $P(0, 31)$ exhibits a highly nonlinear dependence on temperature as can be seen in the left of Fig. 12, leading to a large bias for line pair B in this region near the centerline of the flame. In the outer region of flame where the mean temperature is

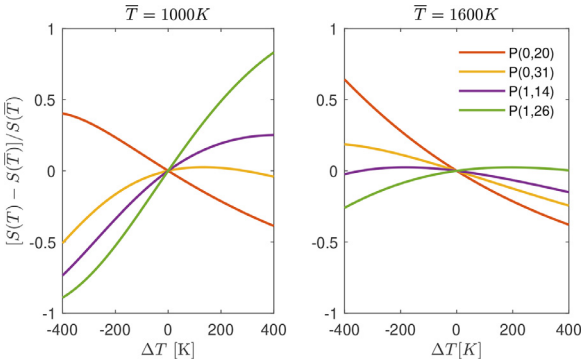

Fig. 12. Normalized linestrength bias of selected transitions as a function of temperature deviation ΔT from two representative mean temperature $\overline{T}$.

higher, all linestrengths scale approximately linearly with temperature, as can be seen in the right of Fig. 12. However, a larger bias in the linestrength of the $P(0, 20)$ transition is observed, resulting in larger bias in temperature for line pairs A and C in this region.

The first-order corrected temperature profiles and corresponding residuals are plotted as dashed lines in Fig. 11. The corrected absorption coefficient $\overline{K}_j$ below 0.01 cm^{-2} near the centerline is too weak to reliably determine temperature, and therefore corrected temperatures in this region are not plotted. Corrected temperature profiles agree well with LES predictions of $\overline{T}$ within 5% across the radial distance for all three line pairs, demonstrating the general usefulness of the first-order correction. Notably, near the centerline of the flame, the corrected temperature profile from line pair C—comprising rovibrational transitions $P(1, 26)$ and $P(0, 20)$—has the lowest residual. This is because the linestrengths of these transitions scale mostly linearly with temperature within this temperature range, as can be seen in the left of Fig. 12.

Based on the preceding analysis, it can be ascertained that when a target flowfield involves correlated scalar fluctuations, it is beneficial to use absorption transitions with linestrengths that scale linearly with temperature over the temperature range of interest, in addition to other line selection criteria for steady uniform flowfields [58]. This conclusion is consistent with the analysis for spatial non-uniformity by Goldenstein et al. [28], recommending use of transitions with linestrengths that are either (1) independent of temperature or (2) that scale linearly with temperature. However, in turbulent flows where the scalar fluctuations and spatial gradients are expected to be sufficiently large, such a requirement for temperature independence over the full range of temperature is less practical.

3.5. Experimental results

In this subsection, we apply the first-order correction to time-averaged laser absorption tomography measurements in a canonical piloted premixed jet flame [24], highlighting the usefulness of the method and additive value of measurements and simulations for a turbulent combustion study. Figure 13 shows representative radial profiles of temperatures determined from experimental time-averaged LAT measurements using line pair B alongside the reference mean temperature profiles $\overline{T}$ from LES predictions at three representative planes. A first-order correction based on the correlation term $\overline{T'X'}_{\text{abs}}$ estimated by temporally and spatially-resolved LES predictions is also plotted for comparison. Experimental error bars are calculated according to the uncertainty analysis described in [24], which includes uncertainty in temperature owing to linestrength uncertainties, residuals from spectral fitting, and uncertainties associated with tomographic reconstruction.

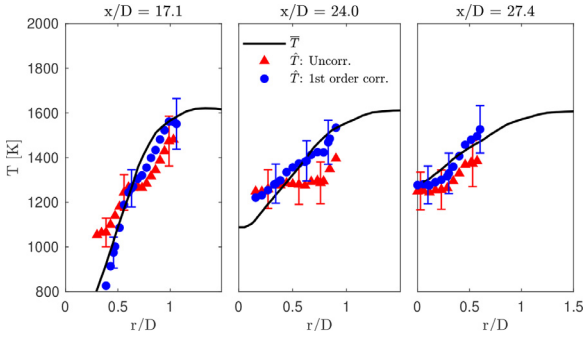

Fig. 13. Temperature profiles obtained from LAT measurements and corresponding simulation predictions and first-order correction at the plane of $x/D = 17.1, 24.0, 27.4$.

Better agreement with LES predictions are achieved after the correction for all three planes. Notably, for the plane at $x/D = 17.1$ the disagreement in temperature near $r/D = 0.3$ is over 200 K without correction, and reduced to 20 K after applying the first-order correction. Similarly, for the plane at $x/D = 27.4$ the temperature disagreement is reduced from 100 K to 20 K near $r/D = 0.5$. This highlights the general usefulness and applicability of the first-order correction on real complex turbulent flowfields. Notably, the biases induced by the correlated scalar fluctuations could be misinterpreted as experimental or modeling errors if not corrected. As such, the first-order correction analysis presented in this work enables more direct comparison between experimental measurements and numerical simulations.

4. Conclusions

In this work, the influence of correlated scalar flowfield fluctuations on inferred thermochemical profiles from time-averaged laser absorption tomography measurements is examined in the context of turbulent piloted premixed flames. Detailed numerical simulations and synthetic data generation reveal that local temperature inferred from typical two-line thermometry methods could lead to a temperature bias of up to 300 K and a CO mole fraction bias up to 0.05 in a piloted premixed jet burner using ethylene-air (which has been the subject of previous studies) [10,11,24]. It is further shown that careful line selection considerations are needed when measuring turbulent flows with highly correlated scalar fields. Namely, it is ideal to use absorption transitions with linestrengths that scale linearly with temperature over the range of the temperature fluctuations. Most notably, a first-order correction to tomography measurements is proposed and applied in both simulated and experimental data in a canonical premixed jet flame to account for the turbulence-induced bias. This method will enable a more direct comparison between time-averaged measurements and numerical simulations, which is crucial for validating combustion models and data assimilation [59]. More broadly, this work establishes a first-order analysis benchmark for time-averaged laser absorption measurements considering correlated flowfield scalar fluctuations and shows the complementary capabilities of high-fidelity reacting flow simulations with quantitative laser absorption diagnostics to study turbulent combustion.

Declaration of Competing Interest

The authors declare that they have no known competing financial interests or personal relationships that could have appeared to influence the work reported in this paper.

Acknowledgments

This work was supported by the Air Force Office of Scientific Research (AFOSR) Young Investigator Program (FA9550-19-1-0062) and grant FA9550-21-1-0077 with Chiping Li as program officer. This research used resources of the National Energy Research Scientific Computing Center, a DOE Office of Science User Facility supported by the Office of Science of the U.S. Department of Energy under Contract No. DE-AC02-05CH11231 using NERSC award BES-ERCAP0021046 and the GCS Supercomputer SuperMUC at Leibniz Supercomputing Centre.

References

[1] E.D. Gonzalez-Juez, A.R. Kerstein, R. Ranjan, S. Menon, Advances and challenges in modeling high-speed turbulent combustion in propulsion systems, Prog. Energy Combust. Sci. 60 (2017) 26–67, doi:10.1016/j.pecs.2016.12.003.
[2] H. Wang, P. Zhang, A unified view of pilot stabilized turbulent jet flames for model assessment across different combustion regimes, Proc. Combust. Inst. 36 (2) (2017) 1693–1703, doi:10.1016/j.proci.2016.06.008.
[3] R. Dibble, R. Hollenbach, Laser rayleigh thermometry in turbulent flames, Symp. (Int.) Combust. 18 (1) (1981) 1489–1499, doi:10.1016/S0082-0784(81)80151-8.
[4] A. Masri, R. Dibble, R. Barlow, The structure of turbulent nonpremixed flames revealed by Raman-Rayleigh-LIF measurements, Prog. Energy Combust. Sci. 22 (4) (1996) 307–362, doi:10.1016/S0360-1285(96)00009-3.
[5] M.J. Dunn, A.R. Masri, R.W. Bilger, A new piloted premixed jet burner to study strong finite-rate chemistry effects, Combust. Flame 151 (1–2) (2007) 46–60, doi:10.1016/j.combustflame.2007.05.010.
[6] M.J. Dunn, A.R. Masri, R.W. Bilger, R.S. Barlow, G.H. Wang, The compositional structure of highly turbulent piloted premixed flames issuing into a hot coflow, Proc. Combust. Inst. 32 (2) (2009) 1779–1786, doi:10.1016/j.proci.2008.08.007.
[7] V. Bergmann, W. Meier, D. Wolff, W. Stricker, Application of spontaneous Raman and Rayleigh scattering and 2D LIF for the characterization of a turbulent CH4/H2/N2 jet diffusion flame, Appl. Phys. B 66 (4) (1998), doi:10.1007/s003400050424.
[8] W. Meier, R.S. Barlow, Y.L. Chen, J.Y. Chen, Raman/Rayleigh/LIF measurements in a turbulent CH4/H2/N2 jet diffusion flame: experimental techniques and turbulence-chemistry interaction, Combust. Flame 123 (3) (2000) 326–343, doi:10.1016/S0010-2180(00)00171-1.
[9] R. Cabra, J. Chen, R. Dibble, A. Karpetis, R. Barlow, Lifted methane-air jet flames in a vitiated coflow, Combust. Flame 143 (4) (2005) 491–506, doi:10.1016/j.combustflame.2005.08.019.
[10] J. Smolke, S. Lapointe, L. Paxton, G. Blanquart, F. Carbone, A.M. Fincham, F.N. Egolfopoulos, Experimental and numerical studies of fuel and hydrodynamic effects on piloted turbulent premixed jet flames, Proc. Combust. Inst. 36 (2) (2017) 1877–1884, doi:10.1016/j.proci.2016.07.127.
[11] F. Carbone, J.L. Smolke, A.M. Fincham, F.N. Egolfopoulos, Comparative behavior of piloted turbulent premixed jet flames of C1–C8 hydrocarbons, Combust. Flame 180 (2017) 88–101, doi:10.1016/j.combustflame.2017.02.030.
[12] L. Paxton, J. Smolke, F.N. Egolfopoulos, Effects of heat release and fuel type on highly turbulent premixed jet flames, Proc. Combust. Inst. 37 (2) (2019) 2565–2572, doi:10.1016/j.proci.2018.08.041.
[13] M. Shimura, T. Ueda, G.M. Choi, M. Tanahashi, T. Miyauchi, Simultaneous dual-plane CH PLIF, single-plane OH PLIF and dual-plane stereoscopic PIV measurements in methane-air turbulent premixed flames, Proc. Combust. Inst. 33 (1) (2011) 775–782, doi:10.1016/j.proci.2010.05.026.
[14] Z. Wang, P. Stamatoglou, B. Zhou, M. Aldén, X.S. Bai, M. Richter, Investigation of OH and CH2O distributions at ultra-high repetition rates by planar laser induced fluorescence imaging in highly turbulent jet flames, Fuel 234 (June) (2018) 1528–1540, doi:10.1016/j.fuel.2018.07.012.
[15] F. Fuest, R.S. Barlow, G. Magnotti, J.A. Sutton, Scalar dissipation rates in a turbulent partially-premixed dimethyl ether/air jet flame, Combust. Flame 188 (2018) 41–65, doi:10.1016/j.combustflame.2017.09.020.
[16] T.A. McManus, J.A. Sutton, Quantitative 2D temperature imaging in turbulent nonpremixed jet flames using filtered Rayleigh scattering, 55th AIAA Aerospace Sciences Meeting, American Institute of Aeronautics and Astronautics, Reston, Virginia (2017), pp. 1–12, doi:10.2514/6.2017-1408.
[17] I. Trueba Monje, J.A. Sutton, Filtered Rayleigh scattering thermometry in premixed flames, 2018 AIAA Aerospace Sciences Meeting, American Institute of Aeronautics and Astronautics, Reston, Virginia, 2018, doi:10.2514/6.2018-1772.
[18] C.S. Goldenstein, R. Spearrin, J.B. Jeffries, R.K. Hanson, Infrared laser-absorption sensing for combustion gases, Prog. Energy Combust. Sci. 60 (2017) 132–176, doi:10.1016/j.pecs.2016.12.002.
[19] W. Cai, C.F. Kaminski, Tomographic absorption spectroscopy for the study of gas dynamics and reactive flows, Prog. Energy Combust. Sci. 59 (2017) 1–31, doi:10.1016/j.pecs.2016.11.002.
[20] C. Wei, D.I. Pineda, L. Paxton, F.N. Egolfopoulos, R.M. Spearrin, Mid-infrared laser absorption tomography for quantitative 2D thermochemistry measurements in premixed jet flames, Appl. Phys. B 124 (6) (2018) 123, doi:10.1007/s00340-018-6984-z.
[21] Z. Wang, T. Kamimoto, Y. Deguchi, W. Zhou, J. Yan, K. Tainaka, K. Tanno, H. Watanabe, R. Kurose, Two dimensional temperature measurement charac-

teristics in pulverized coal combustion field by computed tomography-tunable diode laser absorption spectroscopy, Appl. Therm. Eng. 171 (August 2019) (2020) 115066, doi:10.1016/j.applthermaleng.2020.115066.
[22] J. Emmert, H. Schneider, C. Meißner, E. Sidiropoulos, J.I. Hölzer, T. Seeger, B. Böhm, A. Dreizler, S. Wagner, Characterization of temperature distributions in a swirled oxy-fuel coal combustor using tomographic absorption spectroscopy with fluctuation modelling, Appl. Energy Combust. Sci. 6 (March) (2021) 100025, doi:10.1016/j.jaecs.2021.100025.
[23] L. Ma, K.P. Cheong, K. Duan, C. Yuan, W. Ren, Hybrid constraint multi-line absorption spectroscopy for non-uniform thermochemical measurements in axisymmetric laminar and jet flames, Opt. Lasers Eng. 154 (May 2021) (2022) 107014, doi:10.1016/j.optlaseng.2022.107014.
[24] D.I. Pineda, L. Paxton, N. Perakis, C. Wei, S. Luna, H. Kahouli, M. Ihme, F.N. Egolfopoulos, R.M. Spearrin, Carbon oxidation in turbulent premixed jet flames: a comparative experimental and numerical study of ethylene, n-heptane, and toluene, Combust. Flame 221 (2020) 371–383, doi:10.1016/j.combustflame.2020.08.008.
[25] S.F. Clifford, The classical theory of wave propagation in a turbulent medium, in: J. Strohbehn (Ed.), Laser Beam Propagation in the Atmosphere. Topics in Applied Physics, vol. 25, Springer Berlin Heidelberg (1978), pp. 9–43, doi:10.1007/3540088121_16.
[26] R.J. Hill, S.F. Clifford, R.S. Lawrence, Refractive-index and absorption fluctuations in the infrared caused by temperature, humidity, and pressure fluctuations, J. Opt. Soc. Am. 70 (10) (1980) 1192–1205, doi:10.1364/JOSA.70.001192.
[27] X. Ouyang, P.L. Varghese, Line-of-sight absorption measurements of high temperature gases with thermal and concentration boundary layers, Appl. Opt. 28 (18) (1989) 3979, doi:10.1364/AO.28.003979.
[28] C.S. Goldenstein, I.A. Schultz, J.B. Jeffries, R.K. Hanson, Two-color absorption spectroscopy strategy for measuring the column density and path average temperature of the absorbing species in nonuniform gases, Appl. Opt. 52 (33) (2013) 7950–7962, doi:10.1364/AO.52.007950.
[29] A.P. Nair, D.D. Lee, D.I. Pineda, J. Kriesel, W.A. Hargus, J.W. Bennewitz, S.A. Danczyk, R.M. Spearrin, MHz laser absorption spectroscopy via diplexed RF modulation for pressure, temperature, and species in rotating detonation rocket flows, Appl. Phys. B 126 (8) (2020) 138, doi:10.1007/s00340-020-07483-8.
[30] L. Ma, K.-P. Cheong, H. Ning, W. Ren, An improved study of the uniformity of laminar premixed flames using laser absorption spectroscopy and CFD simulation, Exp. Therm. Fluid Sci. 112 (2020) 110013, doi:10.1016/j.expthermflusci.2019.110013.
[31] N.A. Malarich, G.B. Rieker, Resolving nonuniform temperature distributions with single-beam absorption spectroscopy. Part I: theoretical capabilities and limitations, J. Quant. Spectrosc. Radiat. Transf. 260 (2021), doi:10.1016/j.jqsrt.2020.107455.
[32] N.A. Malarich, G.B. Rieker, Resolving nonuniform temperature distributions with single-beam absorption spectroscopy. Part II: implementation from broadband spectra, J. Quant. Spectrosc. Radiat. Transf. 272 (2021) 107805, doi:10.1016/j.jqsrt.2021.107805.
[33] L. Ma, W. Cai, A.W. Caswell, T. Kraetschmer, S.T. Sanders, S. Roy, J.R. Gord, Tomographic imaging of temperature and chemical species based on hyperspectral absorption spectroscopy, Opt. Express 17 (10) (2009) 8602, doi:10.1364/OE.17.008602.
[34] M.P. Wood, K.B. Ozanyan, Simultaneous temperature, concentration, and pressure imaging of water vapor in a turbine engine, IEEE Sens. J. 15 (1) (2015) 545–551, doi:10.1109/JSEN.2014.2349796.
[35] S.J. Grauer, J. Emmert, S.T. Sanders, S. Wagner, K.J. Daun, Multiparameter gas sensing with linear hyperspectral absorption tomography, Meas. Sci. Technol. 30 (10) (2019) 105401, doi:10.1088/1361-6501/ab274b.
[36] D. Wen, Y. Wang, Spatially and temporally resolved temperature measurements in counterflow flames using a single interband cascade laser, Opt. Express 28 (25) (2020) 37879, doi:10.1364/oe.411278.
[37] C. Shui, Y. Wang, W. Cai, B. Zhou, Linear multispectral absorption tomography based on regularized iterative methods, Opt. Express 29 (13) (2021) 20889, doi:10.1364/oe.421817.
[38] X. Liu, G. Zhang, Y. Huang, Y. Wang, F. Qi, Two-dimensional temperature and carbon dioxide concentration profiles in atmospheric laminar diffusion flames measured by mid-infrared direct absorption spectroscopy at 4.2 μm, Appl. Phys. B 124 (4) (2018) 61, doi:10.1007/s00340-018-6930-0.
[39] K.-P. Cheong, L. Ma, Z. Wang, W. Ren, Influence of line pair selection on flame tomography using infrared absorption spectroscopy, Appl. Spectrosc. 73 (5) (2019) 529–539, doi:10.1177/0003702818815181.
[40] R.K. Hanson, R.M. Spearrin, C.S. Goldenstein, Spectroscopy and optical diagnostics for gases, Springer International Publishing, Cham, 2016, doi:10.1007/978-3-319-23252-2.
[41] C. Wei, K.K. Schwarm, D.I. Pineda, R.M. Spearrin, Volumetric laser absorption imaging of temperature, CO and CO2 in laminar flames using 3D masked Tikhonov regularization, Combust. Flame 224 (2021) 239–247, doi:10.1016/j.combustflame.2020.10.031.
[42] K.J. Daun, K.A. Thomson, F. Liu, G.J. Smallwood, Deconvolution of axisymmetric flame properties using Tikhonov regularization, Appl. Opt. 45 (19) (2006) 4638, doi:10.1364/AO.45.004638.
[43] C.J. Dasch, One-dimensional tomography: a comparison of Abel, onion-peeling, and filtered backprojection methods, Appl. Opt. 31 (8) (1992) 1146, doi:10.1364/AO.31.001146.
[44] D.D. Cox, P.C. Hansen, Rank-deficient and discrete III-posed problems: numerical aspects of linear inversion, J. Am. Stat. Assoc. 94 (448) (1999) 1388, doi:10.2307/2669959.
[45] L. Rothman, I. Gordon, R. Barber, H. Dothe, R. Gamache, A. Goldman, V. Perevalov, S. Tashkun, J. Tennyson, HITEMP, The high-temperature molecular spectroscopic database, J. Quant. Spectrosc. Radiat. Transf. 111 (15) (2010) 2139–2150, doi:10.1016/j.jqsrt.2010.05.001.
[46] M.J. Dunn, A.R. Masri, R.W. Bilger, R.S. Barlow, Finite rate chemistry effects in highly sheared turbulent premixed flames, Flow Turb. Combust. 85 (3–4) (2010) 621–648.
[47] A. Vreman, An eddy-viscosity subgrid-scale model for turbulent shear flow: algebraic theory and applications, Phys. Fluids 16 (10) (2004) 3670–3681, doi:10.1063/1.1785131.
[48] O. Colin, F. Ducros, D. Veynante, T. Poinsot, A thickened flame model for large eddy simulations of turbulent premixed combustion, Phys. Fluids 12 (7) (2000) 1843–1863, doi:10.1063/1.870436.
[49] Y. Khalighi, F. Ham, J. Nichols, S.K. Lele, P. Moin, Unstructured large eddy simulation for prediction of noise issued from turbulent jets in various configurations, 17th AIAA/CEAS Aeroacoustics Conference (32nd AIAA Aeroacoustics Conference) (2011), p. 2886, doi:10.2514/6.2011-2886.
[50] P.C. Ma, Y. Lv, M. Ihme, An entropy-stable hybrid scheme for simulations of transcritical real-fluid flows, J. Comput. Phys. 340 (2017) 330–357.
[51] H. Wu, P.C. Ma, M. Ihme, Efficient time-stepping techniques for simulating turbulent reactive flows with stiff chemistry, Comput. Phys. Commun. 243 (2019) 81–96.
[52] S. Gottlieb, C.-W. Shu, E. Tadmor, Strong stability-preserving high-order time discretization methods, SIAM Rev. 43 (1) (2001) 89–112, doi:10.1137/S003614450036757X.
[53] H. Wang, X. You, A.V. Joshi, S.G. Davis, et al. USC Mech Version II. High-Temperature Combustion Reaction Model of H2/CO/C1-C4 Compounds, 2007, http://ignis.usc.edu/USC_Mech_II.htm.
[54] T. Lu, C.K. Law, A directed relation graph method for mechanism reduction, Proc. Combust. Inst. 30 (1) (2005) 1333–1341, doi:10.1016/j.proci.2004.08.145.
[55] D.G. Goodwin, R.L. Speth, H.K. Moffat, B.W. Weber, Cantera: an object-oriented software toolkit for chemical kinetics, thermodynamics, and transport processes, 2018, (https://www.cantera.org). Version 2.4.0. 10.5281/zenodo.1174508
[56] H. Tennekes, J.L. Lumley, A First Course in Turbulence, The MIT Press, Cambridge, MA, 1972.
[57] R.M. Spearrin, C.S. Goldenstein, I.A. Schultz, J.B. Jeffries, R.K. Hanson, Simultaneous sensing of temperature, CO, and CO2 in a scramjet combustor using quantum cascade laser absorption spectroscopy, Appl. Phys. B 117 (2) (2014) 689–698, doi:10.1007/s00340-014-5884-0.
[58] X. Zhou, J. Jeffries, R. Hanson, Development of a fast temperature sensor for combustion gases using a single tunable diode laser, Appl. Phys. B 81 (5) (2005) 711–722, doi:10.1007/s00340-005-1934-y.
[59] J.W. Labahn, H. Wu, B. Coriton, J.H. Frank, M. Ihme, Data assimilation using high-speed measurements and LES to examine local extinction events in turbulent flames, Proc. Combust. Inst. 37 (2) (2019) 2259–2266, doi:10.1016/j.proci.2018.06.043.